J. Phys. D: Appl. Phys. **41** (2008) 105502 (7pp) doi:10.1088/0022-3727/41/10/105502

Mapping of microwave-induced phonons by μ-Brillouin spectroscopy: hypersons in ZnO on silicon

L Le Brizoual[1,3], J K Krüger[2,3], O Elmazria[1,3], B Vincent[1,3], L Bouvot[1,3], M Kolle[2,3], D Rouxel[1,3] and P Alnot[1,3]

[1] Laboratoire de Physique des Milieux Ionisés et Applications, CNRS-UMR 7040, F-54506, France
[2] Fachrichtung 7.2, Experimentalphysik, Universität des Saarlandes, Bau 38, D-66041 Saarbrücken, Germany
[3] Laboratoire Européen de Recherche Universitaire, Saarland-Lorraine, France

E-mail: laurent.lebrizoual@lpmi.uhp-nancy.fr

Received 28 September 2007, in final form 24 March 2008
Published 25 April 2008
Online at stacks.iop.org/JPhysD/41/105502

Abstract
High performance Brillouin microscopy has been used as a versatile method in order to characterize the spatial distribution of piezoelectrically induced acoustic fields excited at microwave frequencies in a ZnO film deposited on silicon. Filtering properties and acoustic field distribution emitted by inter-digital transducers as well as propagation losses are investigated by μ-Brillouin spectroscopy. It turns out that the acoustic field intensity decreases dramatically outside the immediate excitation area situated below the inter-digital finger structure.

(Some figures in this article are in colour only in the electronic version)

1. Introduction

The last two decades have seen huge development in piezoelectric-based devices such as filters, oscillators or even sensors. In order to improve the efficiency of such devices, two aspects should be explored: the optimization of the material's properties (coupling coefficient, acoustic wave velocity, piezoelectric coefficient, etc) or of the design of the electrodes. Indeed, the coupling between both transducers could be increased to reduce losses. However, this option needs the acoustic field distribution very precisely. Several methods have been developed to achieve this: optical interferometry [1], atomic force microscopy [2], x-ray spectroscopy [3] and scanning electron microscopy [4].

For this type of measurement we have chosen to use Brillouin microscopy. Indeed, Brillouin spectroscopy (BS) is the current technique for measuring acoustic properties at hypersonic frequencies (e.g. [5–7]). Moreover, BS has been proven to be a versatile method for detecting thermally excited surfaces as well as guided acoustic waves at microwave frequencies (e.g. [8–10]). Furthermore, BS was used to determine hypersonic attenuation in quartz from the decay of the Stokes intensity of the Brillouin spectrum on microwave-induced phonons generated at the surface of a piezoelectric crystal [11]. Only recently has BS been used for studying acoustic microscopy (BM) [12, 13]. Finally, the spatial resolution of BM was taken to characterize the mapping of acoustic fields generated by inter-digital transducers (IDTs) on $LiNbO_3$ single crystals [14, 15].

In this paper we investigate microwave-induced sound waves propagating in a thin piezoelectric layer of ZnO, deposited on silicon. The aim of this paper is to measure the electro-acoustic generation of hypersonic waves in thin piezoelectric films, including their acoustic field properties and more especially their spatial decay within the film's plane. Another aspect concerns using BS measurements to study the properties of the pass band frequency for our IDTs within the microwave range.

2. Experimental set-up

2.1. Sample preparation

Owing to their high electromechanical coupling coefficient, ZnO films have been widely investigated as a piezoelectric

material for surface acoustic wave (SAW) devices [16–18]. For our application we have sputtered the piezoelectric ZnO film on a silicon substrate which allows the monolithic integration of the acoustic elements and the associated electronic circuit [18]. Zinc oxide films elaborated by sputtering techniques are very sensitive to deposition parameters: pressure, temperature, gas fraction, the target–substrate distance, etc [19]. The deposition conditions were optimized in order to obtain highly oriented polycrystalline ZnO films. These films were deposited by a dc planar magnetron sputtering system on silicon (1 0 0) substrates. The diameter of the zinc target (purity 99.99%) was 107 mm (4 inch) and the thickness was 6.35 mm. The distance between the cathode and the substrate holder was 80 mm. The deposition chamber was pumped down to a base pressure of 5×10^{-5} Pa by a turbo-molecular pump prior to the introduction of the argon–oxygen gas mixture for ZnO thin film production. The gas discharge mixture was Ar/O_2 and the total pressure was 2×10^{-1} Pa. For an optimum deposition condition, the oxygen percentage in the Ar/O_2 gas mixture was fixed at 70% and the dc power delivered by the dc generator was fixed at 120 W. The substrate and the chamber wall were grounded and the substrate holder was heated to a temperature of 200 °C prior to deposition. The crystallographic properties of the films were analysed by x-ray diffraction (XRD) using Cu Kα radiation. The atomic compositions of the ZnO films were measured by energy dispersive x-ray spectroscopy (EDXS). The structure of the film was characterized by transmission electron microscopy (TEM) with a PHILIPS CM200 microscope operating at an accelerating voltage of 200 kV with an unsaturated LaB_6 cathode. For the electron microscopy studies, a small amount of the thin film was placed on a carbon coated aluminium grid. Both the morphology and the crystallite size of the particles were estimated by TEM bright-field imaging. Structural information was obtained using selected area electron diffraction (SAED) patterns. Our Brillouin spectrometer is based on an argon laser synchronized by Pockel-cells. The scattered light is collected at a 90° angle from the incident beam. A single Fabry–Perot interferometer is used as a frequency filter. A photomultiplier is used to detect the selected light.

2.2. Acoustic wave device characteristics

In order to create an acoustic wave device we deposited two inter-digital finger transducers (IDTs) onto the ZnO film (figure 1). In this experiment the left IDT is used as an emitter and the right one as a receiver. The combination of both the transducers and the piezoelectric thin film characteristics defined the band pass transfer function realized by the device. Figure 1 shows a photograph of the IDT structure on the ZnO film. The IDT was connected by gold wires to the microwave connectors. The gold wires are wedge-bonded to the IDT. The IDT array had a micrometer so that SAWs are generated in the gigahertz regime. The total surface of the array is about $1 \times 1\,\text{mm}^2$. The microwave generator was electrically decoupled from the sample by an isolator. Due to the standing wave ratio of SWR = 2.15, the electromagnetic impedance matching the driving frequency was rather satisfactory.

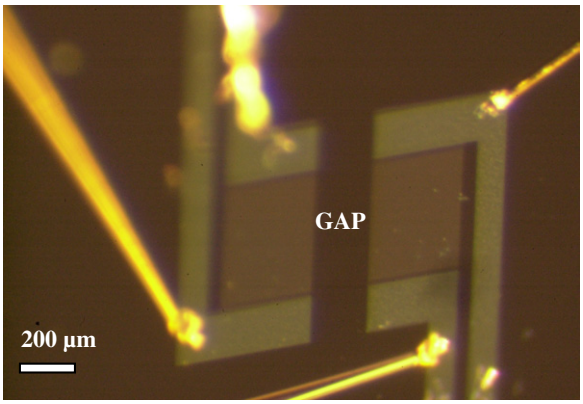

Figure 1. IDT structure on the ZnO film. The IDT is connected by gold wires to microwave connectors.

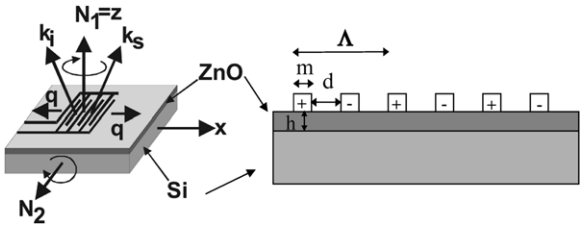

Figure 2. A SAW device with a schematic drawing of the $RI\Theta A$-scattering geometry. $\vec{k}_i$ and $\vec{k}_s$: optical field vector, $\vec{q}$: acoustic wave vector, (x, y, z): sample coordinate system, N_1: rotation axes orthogonal to the film plane, N_2: rotation axis orthogonal to the (x, z)-plane, ZnO: polycrystalline piezoelectric zinc oxide film, Si: silicon substrate.

The geometrical dimensions of the IDTs were as follows: the finger thickness was 1 μm (noted m in figure 2) and the distance between the fingers amounted to 2 μm (noted d in figure 2) yielding a periodic structure of 6 μm (noted Λ in figure 2). The number of IDT fingers was fixed at 50; the IDT thickness is 150 nm. The metallization lateral size is 1 μm and the periodicity is fixed at 6 μm. The ZnO thickness (noted h in figure 2) was fixed at 0.7 μm. The centre frequency f of the acoustic wave device is determined by the acoustic phase velocity V and the wavelength Λ of the IDTs: $f = V/\Lambda$ (figure 2). Consequently, either a material with a high acoustic phase velocity, such as diamond [20, 21], or sub-micrometric lithography could be required in order to increase the basic frequency f of the emitting IDT.

2.3. Brillouin microscopy

In this paper we are looking for microwave-induced SAWs as well as guided bulk waves. Taking into account an acoustic wavelength defined by the scattering geometry of about 2.5 μm and furthermore taking into account that the ZnO film is deposited on a Si substrate, the ZnO film behaves like an acoustic waveguide with the properties very close to that of the bulk material. It is worth noting that we are interested in acoustic wave measurements with the acoustic wave vector perpendicular to the fingers of the IDTs (figure 2).

In order to be able to detect these induced phonons with BS, we adjusted the scattering geometry of the Brillouin experiment in such a way that the wave vector of the

thermal phonon coincides with that of the microwave-induced acoustic wave.

This problem is a difficult one, but can be solved by using the so-called 'reflection-induced ΘA' ($RI\Theta A$)-scattering geometry [22]. In other words, the $RI\Theta A$-scattering geometry enables us to adjust the phonon wave vector involved in the light scattering process in a self-controlled manner precisely parallel to the surface of a film-like transducer at which the hypersonic waves are piezoelectrically excited. Actually, the $RI\Theta A$-scattering geometry is similar to the classical ΘA-scattering geometry [23] for which the acoustic wave vector does not depend on the refractive index of the sample. A simple rotation of the sample around the normal to the excitation surface (N_1 in figure 2) is sufficient to adjust the phonon wave vector defined by the scattering geometry to coincide with that of the piezoelectrically stimulated sound wave. The correct magnitude of this wave vector is adjusted by rotating the sample around the in-plane axis (N_2 in figure 2).

According to figure 2, the Brillouin scattering process at the ZnO/Si interface follows the $RI\Theta A$-scattering geometry [22] where the phonon wave vector is parallel to the silicon surface plane and points along the x-axis of the sample coordinate system introduced in the same figure. The directions of the optical wave vectors $\vec{k}_i$ and $\vec{k}_s$ are also indicated in figure 2. For this 'reflection-induced scattering geometry' the relation between the sound velocity $V^{\Theta A}$ and the sound frequency $f^{\Theta A}$ for a given acoustic wave vector $q^{\Theta A}$ is given by the relation

$$V^{\Theta A} = \frac{2\pi f^{\Theta A}}{q^{\Theta A}} = f^{\Theta A} \cdot \frac{\lambda_0}{2n_i \cdot \sin\left[\frac{\Theta_i}{2}\right]} = f^{\Theta A} \cdot \frac{\lambda_0}{2 \cdot \sin\left[\frac{\Theta}{2}\right]} \tag{1}$$

In equation (1) n_i is the relevant refractive index of the sample, Θ_i is the scattering angle within the sample and Θ is the outer scattering angle [7]. Of course, Θ_i is smaller thanΘ. Using Snellius' law, the last part of equation (1) can be easily verified. Equation (1) is independent of the refractive index n_i [7]. The sagittal angle $\Theta/2$ can be changed experimentally from 0° up to almost 90° by rotating the sample around the axis N_2 (figure 2), which is in the Si-mirror plane. It should be recalled that rotating the sample around N_2 changes the magnitude of the phonon wave vector but not its direction. Of course, $V^{\Theta A}$ is not usually invariant under rotation around N_1, but probes the symmetry in the plane of the sample [7]. For convenience, we worked in the lower gigahertz regime. We therefore chose an outer scattering angle of $\Theta = 12°$, yielding an acoustic phonon wavelength of $\Lambda_p = 2.5\,\mu$m and a frequency of about 2.55 GHz for the longitudinal polarized bulk mode of the undisturbed crystalline state. The scattering geometry was chosen to detect the phonon propagation along the crystallographic x-direction.

It should be stressed that BS (BM) is an extremely sensitive method for probing hypersonic waves: since BM is usually able to detect thermal phonons, every coherently generated phonon will be detected as an excess intensity in the corresponding phonon line within the Brillouin spectrum. The spatial resolution of the BM used for these experiments is about 50 μm, but can be drastically improved [12, 13].

3. Theoretical model

A general finite element calculation is given here for the ac steady state analysis of two-dimensional piezoelectric devices. The method is applied to the SAW in layered structures. In this paper the well-known finite element method (FEM) is applied for analysing the SAWs. Assuming a linear behaviour of the material and steady state sinusoidal time dependence, the quasi-static equations for the modelling of piezoelectric devices are Newton's law, Gauss' law and the constitutive relations as given below, respectively, from equations (2)–(7). The quantities are, respectively, S_{ij}: strain; T_{ij}: stress; E_k: electric field; D_i: dielectric displacement; Φ: electric potential; C_{ijkl}: elastic constant; e_{ikl}: piezoelectric constant; ρ: density; ε_{ij}: dielectric permittivity; u_i: mechanical displacement. More details of the theoretical aspect are given in [8–10]. In a two-dimensional model, no variation was permitted in the N_2 direction (figure 2). As we are interested in the harmonic response of the device, the governing differential equations which define the mechanical and the electrical properties in the volume have to be established for the amplitudes of the mechanical displacement u_i (only in the N_1 and N_3 directions, figure 2) and the electrical scalar potential Φ in equations (8) and (9):

$$S_{ij} = \frac{1}{2}\left(\frac{\partial u_i}{\partial x_j} + \frac{\partial u_j}{\partial x_i}\right), \tag{2}$$

$$T_{ij} = \sum_{k,l} C_{ijkl} S_{kl} - \sum_k e_{kij} E_k \qquad k, l = 1, 2, 3, \tag{3}$$

$$D_i = \sum_{k,l} e_{ikl} S_{kl} + \sum_k \varepsilon_{ik} E_k \qquad k, l = 1, 2, 3, \tag{4}$$

$$E_i = -\frac{\partial^2 \Phi}{\partial x_i}, \tag{5}$$

$$\frac{\partial T_{ij}}{\partial x_j} = \rho \frac{\partial^2 u_i}{\partial^2 t}, \tag{6}$$

$$\frac{\partial D_i}{\partial x_i} = 0, \tag{7}$$

$$\sum_{j,k,l} C_{ijkl} \frac{\partial^2 u_j}{\partial x_j \partial x_i} + \sum_{j,k} e_{kij} \frac{\partial^2 \Phi}{\partial x_j \partial x_k} = \rho \frac{\partial^2 u_i}{\partial^2 t}, \tag{8}$$

$$\sum_{k,l} e_{ikl} \frac{\partial^2 u_l}{\partial x_j \partial x_k} - \sum_k \varepsilon_{ik} \frac{\partial^2 \Phi}{\partial x_i \partial x_k} = 0. \tag{9}$$

Besides these two sets of linear equations (7) and (8), we further evaluate the integral quantities, such as the electrical input impedance characterizing our piezoelectric device. The input impedance of a piezoelectric transducer also reveals all the resonances and antiresonances of the device. The resonances are the natural frequencies for short-circuited electrodes, while the antiresonances are those for open-circuit conditions. To compute the electrical input impedance of a piezoelectric transducer with the finite element method, the transducer has to be excited by a harmonic frequency and the integral calculation results can be used to quantify the mechanical and electrical responses, for example, the displacement of a region of interest, such as the surface of the

Table 1. Material constants.

Material	Silicon	ZnO
Elastic constant (10^{11} N m^{-2})	1.66	2.1
C_{11}	0.639	1.25
C_{12}	0.639	1.05
C_{13}	0.795	0.425
C_{44}		
Piezoelectric constant (C m^{-2})		
e_{13}	—	−0.61
e_{33}	—	1.14
e_{15}	—	−0.51
Relative dielectric constant		
ε_{11}	11.8	8.34
ε_{33}	11.8	8.84
Density ρ (kg m^{-3})	2329	5676

device for Rayleigh waves. With these results the propagation mode is easy to determine by counting the number of nodes belonging to the N_3 direction displacement, which directly gives the harmonic order of the propagating wave. Although the model can treat intrinsic material losses as imaginary parts of the physical constants, these leakage sources have been neglected in this work because almost no data are available concerning ZnO or silicon (which is assumed to be one of the principal leakage sources of the device). The only leakage phenomena that can occur are, then, related to wave radiation into the bulk, which are absorbed by a dedicated layer in the model. This layer absorbs the bulk. Using the material constants given in table 1, the model provides electrical and mechanical deformations of the layered structure. We assume a constant polarization of 1 V on the aluminium electrode.

4. Results and discussions

The XRD results observed on a 1 μm thick ZnO film give a (0 0 2) reflection corresponding to the *c*-axis perpendicular to the substrate. Figure 3(*a*) shows the XRD spectra of the ZnO film deposited on silicon. The peak at 34.4 corresponds to the (0 0 2) diffraction line of the ZnO wurtzite structure. This spectrum corresponds to a film with the *c*-axis perpendicular to the surface. In comparison with the location of the (0 0 2) reflection of a single crystal, within the polycrystalline sample, a slight shift is observed and is attributed to an increase in the compressive stress within the film plane. As expected, the EDXS measurements reflect the stoichiometry of Zn_1O_1. Figure 3(*b*) shows a typical TEM image of the as-deposited sample and the corresponding SAED pattern (figure 3(*c*)). Figure 3(*b*) shows that the ZnO nanocrystallites are well oriented, in a columnar structure. The diffraction rings in figure 3(*c*) correspond to the ZnO plane. The approximate lateral size of the ZnO columns varies according to the TEM micrograph from 20 to 50 nm.

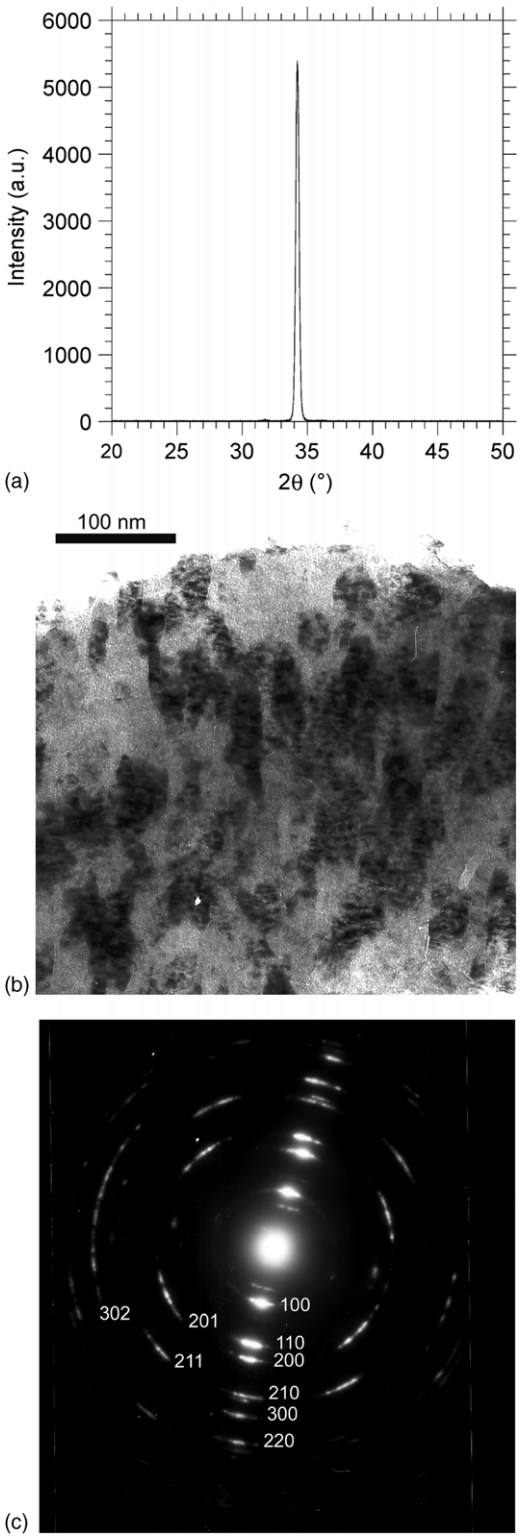

Figure 3. The TEM results on ZnO films deposited at 2×10^{-1} Pa, respectively, with 70% of oxygen in the Ar/O_2 gas mixture: (*a*) XRD spectra, (*b*) ZnO micrograph and (*c*) ZnO electron diffraction pattern.

4.1. Modelization (results of the theoretical calculations) results

Figure 4 shows the admittance of the device as a function of the frequency. As can be seen, the device presents several resonances.

The resonance frequencies are, respectively, 0.632 GHz, 0.937 GHz, 1.52 GHz, 2.31 GHz and 2.43 GHz attributed to the fundamental and harmonic modes. The theoretical model also gives the elastic shape of those modes. Mode 0 harmonic 1 (a) is called M0H1, and the corresponding elastic shape is shown

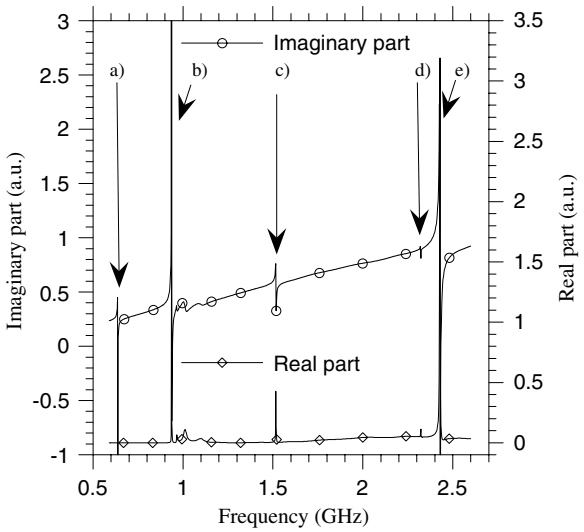

Figure 4. Real and imaginary parts of the admittance of the device obtained by the theoretical calculation. The periodicity was 6 μm and the IDT thickness was 150 nm. The ZnO thickness was fixed at 700 nm. The mode order X and the harmonic order Y was noted as MXHY: (a) M0H1, (b) M1H1, (c) M0H3, (d) M0H5 and (e) M1H3.

in figure 5(*a*). This mode essentially propagates at the top of the surface and presents a depth penetration length lower than one wavelength. Mode 1, figure 5(*b*), has a larger penetration depth than mode 0 and has a larger deformed area in the silicon. This mode is particularly adapted to BS due to its high frequency of propagation (near 1 GHz) and its high intensity on the frequency response (figure 4). All other modes are harmonic modes of modes 0 and 1. The higher advantageous modes are mode 0 harmonic 3 (c) and mode 1 harmonic 3 (e), which present a relatively higher intensity on the frequency response compared with the others.

4.2. BS characterization

BS was performed on the device described above in order to characterize the distribution of the microwave-induced acoustic field propagating in the layered structure. We have studied the pass band frequency behaviour of the emitting IDT (left IDT in figure 1) on polycrystalline ZnO by BM.

The thermal phonon spectrum was first measured for an outer scattering angle of 12° (figure 6). The thermal phonon spectrum of figure 6 is widely spread out; consequently separated phonon lines are not observed. Taking into account that the ZnO film is polycrystalline and the build-up of nano-sized grains, the measured spectrum reflects an orientational averaging over many crystallites within the scattering volume. The averaged state should yield two phonon modes related to a material with isotropic symmetry. These two spectral features are not resolved in the spectrum as expected. A likely explanation for this broadening of the line could be an excessive hypersonic attenuation. Grain boundaries and/or clusters of nano-grains within the polycrystalline ZnO film are believed to be the cause of this strong acoustic attenuation.

As a consequence of this strong attenuation, we were not sure to be able to detect any induced phonon at all in the sample. Of course, if there were any, they would be found

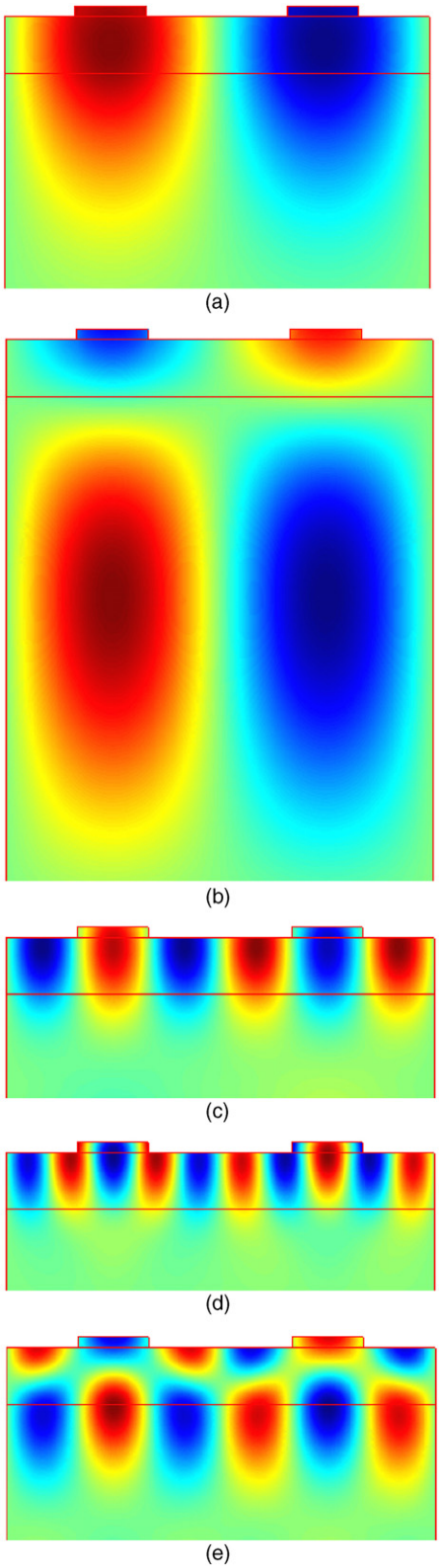

Figure 5. Deformation shape given by the theoretical calculation. The mode order and the harmonic 1: (*a*) M0H1, (*b*) M1H1, (*c*) M0H3, (*d*) M0H5 and (*e*) M1H3.

in the area below the emitting IDT, where the acoustic signal is created by electro-acoustic coupling. Therefore, we adjusted the scattering volume directly on the IDT and discovered the microwave-induced phonon lines that we were looking for.

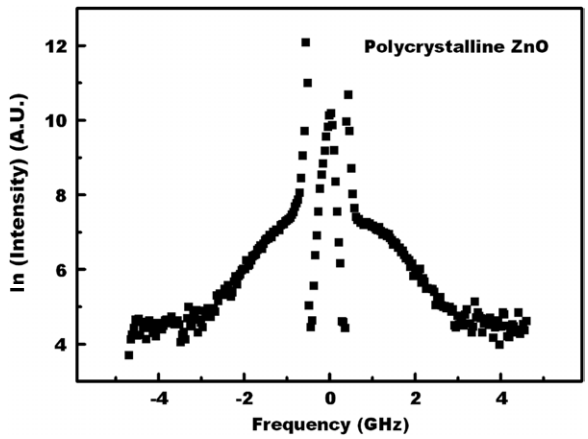

Figure 6. Brillouin spectrum in the logarithmic scale of the thermal phonons measured at an outer scattering angle of 12° in a 700 nm thin ZnO film deposited on silicon and measured with the $RI\Theta A$-scattering geometry.

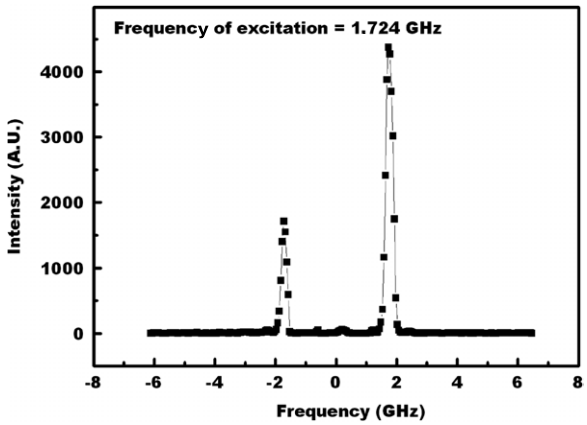

Figure 7. Microwave-induced Brillouin intensities of the Stokes and anti-Stokes lines measured on a ZnO film deposited on a silicon substrate. The exciting microwave frequency is $f_{MW} = 1.724$ GHz.

Table 2. Phonon lines frequencies.

f_{IDT} (GHz)	0.953	1.724	2.203	2.385	2.592	2.898

Figure 7 shows an example of induced phonon lines. The asymmetry between the Stokes and anti-Stokes lines comes from the fact that the point of analysis is not located exactly in the centre of the IDT.

First of all, we determined the pass band behaviour of our device by varying the applied frequency on our IDTs and simultaneously detecting the induced phonons on the Brillouin spectrum. We then obtained huge phonon lines for several frequencies that are summarized in table 2. If we compare these BS results with the theoretical ones and with electrical measurements, we can attribute each frequency to modes and harmonics that can be generated by our device.

Our electrical results, are of course, less sensitive than the Brillouin measurements, which is the reason why some modes are detectable with BS, but not with electrical measurements by reflection. However, these results are difficult to explain. Indeed, theoretically, the different orders vary in wavelength and so cannot be detected by Brillouin measurements with the same angle of scattering that defines the length of a detectable wavelength. A possible explanation is that the IDT acts as an optical grating and hence induces many orders of diffraction under the IDTs. Consequently, we would not have only one angle of incidence, but several, caused by the different orders of diffraction. Moreover, the numerical aperture of the collection lens contributes to enhancing the number of detectable wavelengths.

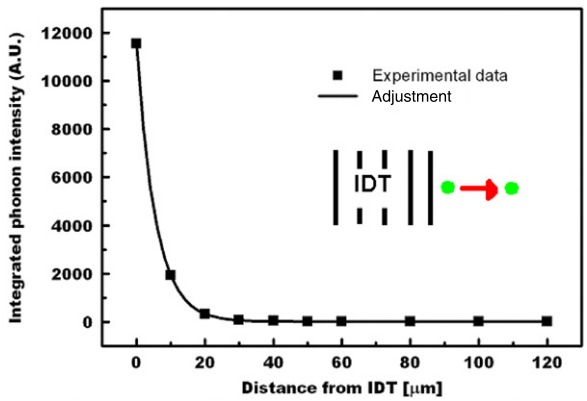

Figure 8. Propagation losses measurement: induced phonon intensity as a function of the propagation distance (applied frequency = 953 MHz).

Next, we studied the spatial distribution of the piezoelectrically excited acoustic field between the emitter and the receiver. It must be noted that, during these measurements, the receiver was short-circuited, in order to avoid any possible disturbance by the electromagnetic coupling between the receiver and the emitter. Indeed, some of our experiments have shown that a large part of the electric energy is electromagnetically radiated by the IDT; so the electromagnetic field can be coupled directly onto the receiver. In such cases, the receiver acts as a second emitter and thus disturbs the measurements of the acoustic field between the electrodes. The acoustic wave amplitude decreases exponentially when propagating out of the IDTs (figure 8). There is a lot of spatial decay for the acoustic wave emitted by the IDT. Propagation losses have been estimated to be 200 mm^{-1}. This value is one order of magnitude higher than the one given by previous authors [18], but confirms the thermal Brillouin spectrum given in figure 6.

We also wanted to study the beam shape of the acoustic wave emitted by the IDTs. So, we have then reproduced the same experiment perpendicularly to the direction of propagation (figure 9). The results showed that the divergence is weak at a short distance from the IDTs because the width of the defined beam is similar to the aperture of the IDTs. This result is in agreement with previous experiments that we performed using lithium niobate single crystal as piezoelectric media. However, it confirms that there is no scattering enhancement due to the nano-crystalline texture, even if acoustic losses remain at a high value.

5. Conclusion

Brillouin microscopy was used as a versatile technique to characterize the field distribution of microwave-induced

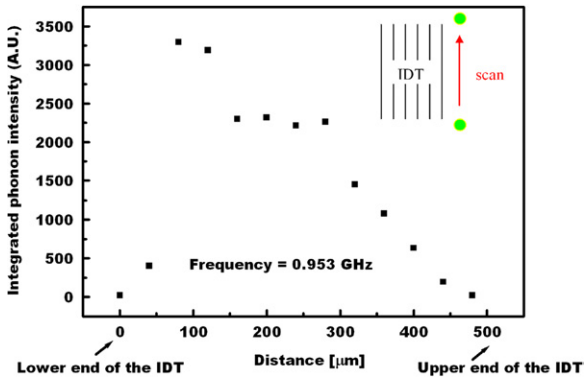

Figure 9. Beam shape visualization. Induced phonon intensity versus the distance perpendicularly to the propagation direction (applied frequency = 953 MHz).

phonons in a thin layer of piezoelectric polycrystalline ZnO deposited on silicon. The electrical resonance behaviour of our device has been studied theoretically and experimentally. Frequencies that are efficiently emitted, that is to say, which correspond to the condition of constructive interference, have been compared with theoretical calculations. All frequencies that gave us a signal under the IDTs were identified in terms of mode and harmonic characteristics. A comparison of the propagation properties of thermal and induced phonons shows drastic hypersonic attenuation behaviour of this polycrystalline material. We have also identified the acoustic beam shape and deduced that the divergence of the beam remains very weak.

Acknowledgments

This work has been supported by the 'Region Lorraine, CONTRAT DE PLAN ETAT-REGION 2000–2006; Pôle de Recherche Scientifique et Technologique, Ingénierie de conception de produits, de matériaux et procédés : Nouveaux matériaux fonctionnels et microtechnologies'. The authors wish to acknowledge L Bouvot and J-F Pautex for their helpful contributions.

References

[1] Monchalin J-P 1985 *Appl. Phys. Lett.* **47** 14
[2] Hesjedal T and Behme G 2001 *IEEE Trans. Ultrason. Ferroelectr. Freq. Control* **48** 641
[3] Whatmore R W, Goddard P A and Tanner B K 1982 *Ultrasonics Symp. Proc.* vol 1, pp 363–6
[4] Roshchupkin D V and Brunel M 1994 *IEEE Trans. Ultrason. Ferroelectr. Freq.Control* **41** 512
[5] Gonzalo J A, de Frutos J and Garcia J 2002 *Solid State Spectroscopy* (Singapore: World Scientific)
[6] Chu B 1974 *Laser Light Scattering* (New York: Academic)
[7] Krüger J K 1989 *Optical Techniques to Characterize Polymer Systems* ed H Bässler (Amsterdam: Elsevier)
[8] Sandercock J R 1982 Trends in Brillouin scattering *Light Scattering in Solids* ed M Cardona and G Guntherodt (Berlin: Springer) p 173
[9] Mutti P, Bottani C E, Ghislotti G, Beghi M, Briggs G A D and Sandercock J 1995 *Advances in Acoustic Microscopy* vol 1 (New York: Plenum)
[10] Hotz R, Krüger J K, Possart W and Tadros-Morgane R 2001 *J. Phys.: Condens. Matter* **13** 7953–67
[11] Krüger J K and Unruh H-G 1977 *Solid State Commun.* **21** 583–6
[12] Sanctuary R, Bactavatchalou R, Müller U, Possart W, Alnot P and Krüger J K 2003 *J. Phys. D: Appl. Phys.* **36** 2738
[13] Krüger J K, Possart W, Bactavachalou R, Müller U, Britz T, Sanctuary R and Alnot P 2004 *J. Adhes.* **80** 585–99
[14] Krüger J K, Vincent B, Elmazria O, Bouvot L and Alnot P 2004 *New J. Phys.* **6** 57
[15] Vincent B, Krüger J K, Elmazria O, Bouvot L, Mainka J, Sanctuary R, Rouxel D and Alnot P 2005 *J. Phys. D: Appl. Phys.* **38** 2026–30
[16] Martin S J, Gunshor R L and Pierret R F 1980 *Appl. Phys. Lett.* **37** 700
[17] Hickerwell F S 1985 *IEEE Trans. Son. Ultrason.* **32** 621
[18] Vellekoop M, Visser C, Sarro P and Venema A 1990 Compatibility of zinc oxide with silicon IC processing *Sensors Actuators* A **21–23** 1027–30
[19] Krupanidhi S B and Sayer M 1984 *J. Appl. Phys.* **56** 3308
[20] Shikata S, Nakahata H, Hachigo A and Fujimori N 1993 *Diamond Relat. Mater.* **2** 1197–202
[21] Lamara T, Belmahi M, Elmazria O, Le Brizoual L, Bougdira J, Remy M and Alnot P 2004 *Diamond Relat. Mater.* **13** 581–4
[22] Krüger J K, Embs J, Brierley J and Jimenez R 1998 *J. Phys. D: Appl. Phys.* **31** 1913
[23] Krüger J K, Marx A, Peetz L, Roberts R and Unruh H-G 1986 *Colloid Polym. Sci.* **264** 403–14